

A code to Make Your Own Synthetic ObservaTionS (MYOSOTIS)

Zeinab Khorrami ¹, ¹★ Pouria Khalaj ², ²★ Anne S. M. Buckner, ³ Paul C. Clark, ¹
Estelle Moraux, ² Stuart Lumsden, ³ Isabelle Joncour, ^{2,4} René D. Oudmaijer, ³
Ignacio de la Calle, ⁵ José M. Herrera-Fernandez, ⁵ Frédérique Motte, ²
José Manuel Blanco ⁵ and Luis Valero-Martin ⁵

¹School of Physics and Astronomy, Cardiff University, The Parade, Cardiff CF24 3AA, UK

²Université Grenoble Alpes, CNRS, IPAG, F-38000 Grenoble, France

³School of Physics and Astronomy, University of Leeds, Leeds LS2 9JT, UK

⁴Department of Astronomy, University of Maryland, College Park, MD 20742, USA

⁵Quasar Science Resources, S.L., Edificio Ceudas, Ctra. de La Coruña, Km 22.300, E-28232 Las Rozas de Madrid, Madrid, Spain

Accepted 2019 February 13. Received 2019 February 13; in original form 2018 February 26

ABSTRACT

We introduce our new code MYOSOTIS (Make Your Own Synthetic ObservaTionS) which is designed to produce synthetic observations from simulated clusters. The code can synthesize observations from both ground- and spaced-based observatories, for a range of different filters, observational conditions and angular/spectral resolution. In this paper, we highlight some of the features of MYOSOTIS, creating synthetic observations from young massive star clusters. Our model clusters are simulated using NBODY6 code and have different total masses, half-mass radii, and binary fractions. The synthetic observations are made at the age of 2 Myr with Solar metallicity and under different extinction conditions. For each cluster, we create synthetic images of the *Hubble Space Telescope* (*HST*) in the visible (WFPC2/*F555W*) as well as Very Large Telescopes in the nearIR (SPHERE/IRDIS/*K_s*). We show how MYOSOTIS can be used to look at mass function (MF) determinations. For this aim we re-estimate stellar masses using a photometric analysis on the synthetic images. The synthetic MF slopes are compared to their actual values. Our photometric analysis demonstrate that depending on the adopted filter, extinction, angular resolution, and pixel sampling of the instruments, the power-law index of the underlying MFs can be shallower than the observed ones by at least ± 0.25 dex which is in agreement with the observed discrepancies reported in the literature, specially for young star clusters.

Key words: instrumentation: adaptive optics – instrumentation: high angular resolution – techniques: photometric – telescopes – stars: luminosity function, mass function – open clusters and associations: general.

1 INTRODUCTION

We have been using *N*-body models to study the physics of star clusters since Van Albada (van Albada 1968). Such simulations have been used to look at stellar cluster core oscillations (Giersz & Heggie 2009; Heggie & Giersz 2009; Hurley & Shara 2012), stellar collisions (Chatterjee, Fregeau & Rasio 2009), merging of star clusters (Priyatikanto et al. 2016), the evolution of multiple systems (Hurley, Tout & Pols 2002) and substructures (Allison et al. 2009), and the phenomenon of mass segregation and its role in cluster evolution (e.g. Portegies Zwart, McMillan & Gieles 2010). Through

this work, the community has built up a picture of how clusters evolve (e.g. Kalirai & Richer 2010), and how this may affect the initial mass function (IMF; e.g. Kroupa 2001). They have also been used to place constraints on the star formation process (e.g. Parker & Reggiani 2013) and how cluster dynamics can affect the stability of planetary systems (e.g. Cai et al. 2017).

The results from *N*-body modelling have been used to help interpret the results from observational studies. For example the evolution of mass function (MF) slope in globular clusters (Baumgardt, De Marchi & Kroupa 2008), relation between the MF slope and the core radius of the star cluster (De Marchi, Paresce & Pulone 2007), and the debate on the observed mass-segregation (primordial, dynamical or observational bias) and its origin in star

* E-mail: khorramiz@cardiff.ac.uk (ZK); paul.clark@astro.cf.ac.uk (PK)

clusters (Espinoza, Selman & Melnick 2009; Bastian, Covey & Meyer 2010; Parker et al. 2016; Domínguez et al. 2017).

Although comparisons between observations and simulations are often made directly to the N -body results, such a comparison is dangerous since:

(i) Most of the young star clusters (YSCs) contain hot and massive stars, which can mask the faint low-mass stars. This leads to an underestimation of the number of low-mass stars which makes the observed MF steeper than the underlying MF at the low-mass end.

(ii) YSCs are immersed in their natal cloud (Lada & Lada 2003; Portegies Zwart et al. 2010) meaning that stellar members suffer from extinction which varies from point to point. This means that applying a constant value of extinction to the entire stellar population inside the cluster leads to an incorrect estimation of stellar masses, and consequently a deformed MF.

(iii) Individual members are not fully resolved for most known YSCs due to their typically large distances. This is especially important for unresolved multiple stars (e.g. binaries) which can affect the measured low- and high-mass slopes of the MF (e.g. Malkov & Zinnecker 2001; Khalaj & Baumgardt 2013).

Considering all the aforementioned observational difficulties, we need to observe YSCs with better angular resolutions and high contrast imaging and preferentially at longer wavelengths. Furthermore, numerical simulations and models of YSCs are dictated and evolve according to observations, but the comparison of the two is far from straightforward. In particular, we always need to take an intermediate step to create synthetic observations from the simulations first, and only then the comparison with the observations is sensible.

In this paper we introduce our code MYOSOTIS (Make Your Own Synthetic Observations), a tool for creating synthetic observational data which produces the imaging and spectroscopic data for space- and ground-based telescopes. Using MYOSOTIS one can change the angular resolution of the observing instrument, pixel sampling of the detector, extinction and the atmospheric conditions. These factors significantly affect the photometric analysis of the individual stars detected in the field of view (FOV), especially in crowded field images like star clusters.

MYOSOTIS enables us to create synthetic images/spectra of telescopes such as the *Hubble Space Telescope* (*HST*), Very Large Telescopes (VLT), and *Gaia*, from the N -body simulations, to be compared with real data of the aforementioned telescopes. Moreover, our tool can be used with custom configurations, meaning that it can replicate the observations of a wide variety of instruments.

MYOSOTIS has been developed as part of the StarFormMapper¹ (SFM) project, which aims to study massive stars and star cluster formation using *Gaia* and *Herschel* data. To this end, we aim to examine how synthetic observations from different telescopes produce different results on the MF of YSCs, and whether it is possible to attribute the observed discrepancy in the MFs of YSCs to different observational conditions.

This paper has two main parts: (1) detailed description of how MYOSOTIS works (Section 2) and (2) examples of the application of the code (Section 3). In the latter part we use MYOSOTIS to create synthetic *HST*/WFPC2 and VLT/SPHERE images of YSCs in the visible (V band) and near-IR (K_s band) from N -body simulations. The details of the N -body simulations are given in Section 3.1. The

synthetic observational data which are created by MYOSOTIS are explained in Section 3.2. In Section 3.3 we explain the photometric method that we used to analyse the synthetic images, extract stellar sources, and finally estimate their masses. One example of synthetic spectroscopic data is given in Section 3.4. A discussion and summary of the results is presented in Section 4.

2 MYOSOTIS: MAKE YOUR OWN SYNTHETIC OBSERVATIONS

This code creates synthetic imaging and spectroscopic data of space- and ground-based telescopes as well as custom (user-defined) instruments within any FOV. The stellar and interstellar medium information (position, mass, velocity, metallicity, age) should be provided by the user. The user can choose different filters from a list (see <http://svo2.cab.inta-csic.es/theory/fps/>; Rodrigo & Solano 2013; Rodrigo et al. 2012) or define a new filter, to suit the observational instrument that they want to mimic. The observing conditions, i.e. seeing, Strehl-Ratio (SR), detector’s pixel scale of a given instrument, FOV, observer’s line of sight and finally the angular resolution of the telescope can be defined in MYOSOTIS. Since most of the instruments cannot achieve their theoretical optimum resolution ($\sim \lambda/\text{diameter}$), the user can also define their own resolution. The estimated flux of stellar sources spreads on the detector using a 2D point spread function (PSF) whose full width at half-maximum (FWHM) is equal to the resolution. The user can choose a Gaussian distribution or an Airy pattern for the PSF of stellar sources. The extinction can be applied on the output data, knowing the column density of the gas in front of each source. This extinction could be uniform, patchy, or taken from a full 3D smoothed particle hydrodynamics (SPH) simulation data.

2.1 Stellar evolutionary and atmosphere models

One of the input files for MYOSOTIS is the information on stellar positions, velocities, masses, ages, and metallicities. For each star, according to its age, metallicity, and mass, MYOSOTIS finds the closest stellar parameters, i.e. effective temperature (T_{eff}), surface gravity ($\log g$), and luminosity ($\log L$), using the grids of PARSEC² evolutionary models (Bressan et al. 2012; Chen et al. 2014, 2015; Tang et al. 2014). PARSEC has a complete theoretical library that includes the latest set of stellar phases from pre-main sequence to main sequence, covering stellar masses from 0.09 to 350 M_{\odot} and ages between 0.1 Myr up to 10.1 Gyr.

After finding T_{eff} and $\log g$ for each star, MYOSOTIS finds the closest stellar atmosphere model that is, the full spectral energy distribution (SED), that fits the given metallicity, T_{eff} and $\log g$ of that star. MYOSOTIS uses the grids of NEXTGEN2 atmosphere models for very low mass stars and brown dwarfs with $900 \text{ K} < T_{\text{eff}} < 3400 \text{ K}$ covering $\log g$ from 3.5 to 6.0 (Allard et al. 1997; Hauschildt, Allard & Baron 1999), and ATLAS9 KURUCZ ODFNEW/NOVER atmosphere models (Castelli, Gratton & Kurucz 1997) for $3500 \text{ K} < T_{\text{eff}} < 50\,000 \text{ K}$ covering $\log g$ from 0.0 to 5.0 for solar metallicity.

Users can choose a specific atmosphere model for hot and massive O- and B-type stars by setting the OB treatment parameter to ‘yes’ (i.e. **OBtreatment = ‘yes’**). In this case, for stars with

¹<http://sfm.leeds.ac.uk>

²We have used PARSEC isochrones (version 1.2S) and CMD 3.0 web interface available at <http://stev.oapd.inaf.it/cgi-bin/cmd>

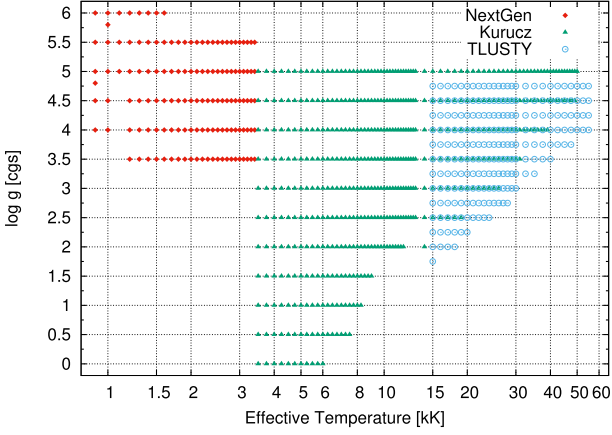


Figure 1. The stellar parameters of the atmosphere models used in MYOSOTIS.

$T_{\text{eff}} > 15\,000\text{ K}$, MYOSOTIS uses the grids of TLUSTY³ atmosphere models (Hubeny & Lanz 1995) for B-type (Lanz & Hubeny 2007) and O-type (Lanz & Hubeny 2003) stars. TLUSTY grids, cover T_{eff} from 15 000 K up to 55 000 K and $\log g$ from 1.75 up to 4.75. Fig. 1 shows the stellar parameters covered by these atmosphere models for solar metallicity. After selecting the appropriate SED for each star, MYOSOTIS will estimate the stellar flux and extinction in a given filter, according to its distance from the observer. In addition to the aforementioned models for stellar evolution and atmospheres, users can define their own customized models and any attenuating dust that has been prescribed by the user.

2.2 Bolometric corrections and extinction

To estimate the bolometric correction (BC) of stars in different filters, we used the method explained in Girardi et al. (2002), i.e. for a given filter BC is given by

$$\text{BC}_{S_\lambda} = M_{\text{bol},\odot} - 2.5 \log[4\pi(10\text{ pc})^2 \sigma T_{\text{eff}}^4 / L_\odot] + 2.5 \log \left[\frac{\int_{\lambda_1}^{\lambda_2} \lambda F_\lambda 10^{-0.4A_\lambda} S_\lambda d\lambda}{\int_{\lambda_1}^{\lambda_2} \lambda f_\lambda^0 S_\lambda d\lambda} \right] - m_{S_\lambda}^0. \quad (1)$$

In this equation, $M_{\text{bol},\odot} = 4.83$ and $L_\odot = 3.828 \times 10^{33} \text{ erg s}^{-1}$. A_λ is the extinction at wavelength λ and S_λ is the filter transmission curve corresponding to the interval $[\lambda_1, \lambda_2]$. F_λ is the stellar intrinsic spectra at wavelength λ which is provided by the atmosphere model for a given T_{eff} , $\log g$ and metallicity. f_λ^0 is the reference spectra of Vega at the Earth surface⁵ that produces a known apparent magnitude $m_{S_\lambda}^0$ in different wavelengths. Vega has $V = 0.034$ mag (3670 Jy for $V = 0$), and all colours are equal to 0. For the Vega spectrum we used synthetic ATLAS9 model, with $T_{\text{eff}} = 9550\text{ K}$, $\log g = 3.95$, and $[M/H] = -0.5$ provided by Castelli et al. (1997).

2.3 Cloud column density

The column density of the cloud in front of each stellar source (uniform or patchy) can be given directly by the user or MYOSOTIS

³<http://nova.astro.umd.edu/Tlusty2002/tlusty-frames-cloudy.html>

⁴'Sun Fact Sheet' <https://nssdc.gsfc.nasa.gov/planetary/factsheet/sunfact.html>

⁵http://basti.oa-teramo.inaf.it/BASTI/MAG_ML/Vega.sed

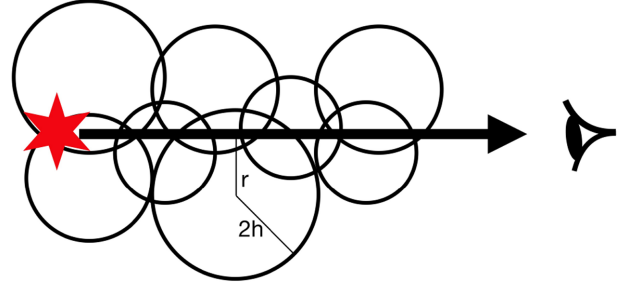


Figure 2. The cloud particles distributed in front of an stellar source. Each cloud particle has a smoothing length (h) and the column density is calculated as a function of r for the particles lying in the line of sight using the kernel function given in equation (2).

can calculate it using the SPH data if it is available. In the case of SPH data, the gas cloud can be located anywhere around the stellar sources as well as anywhere within the line of sight of the observer. MYOSOTIS then calculates the cloud column density in front of each star (in the line of sight of the observer). The user should provide the cloud information (cloud particles positions, mass, and smoothing lengths). This information is the standard output of the SPH simulations. In SPH, particle properties are smoothed over a length scale, h , called the smoothing length, using a weighting function, $W(r, h)$, called the kernel function. MYOSOTIS uses M4 cubic spline kernel function (Monaghan & Lattanzio 1985), shown in equation (2).

$$W(r/h) = \frac{1}{\pi h^3} \begin{cases} 1 - \frac{3}{2}(r/h)^2 + \frac{3}{4}(r/h)^3 & 0 \leq r/h \leq 1 \\ \frac{1}{4}(2 - r/h)^3 & 1 \leq r/h \leq 2 \\ 0 & 2 \leq r/h \end{cases} \quad (2)$$

Fig. 2 is a schematic representation of the cloud particles distributed in front of a stellar source. MYOSOTIS detects the cloud particles which are located in the line of sight of the observer and the stellar source. Each cloud particle has a smoothing length and a mass. The column density of the cloud can be calculated using the kernel function (equation 2), as a function of distance from the centre of each cloud particle and its mass. After estimating the column density in front of each star, we use the relation between optical extinction (A_V) and hydrogen column density N_H [cm^{-2}] from Güver & Özel (2009), i.e.

$$N_H (\text{cm}^{-2}) = (2.21 \pm 0.09) \times 10^{21} A_V (\text{mag}). \quad (3)$$

2.4 Extinction

The extinction for each stellar source can be calculated using two different methods:

(i) **Fmodel:** The code uses a function to calculate extinction in a given wavelength knowing optical extinction values (A_V and R_V). This function uses the average extinction curve in the optical-through-IR range (0.125–3.333 μm) which is reproduced with a cubic spline and a set of anchor points from Fitzpatrick (1999).

(ii) **Dmodel:** The code uses synthetic extinction curves⁶ from Draine (2003a,b,c), Li & Draine (2001), and Weingartner & Draine (2001). Extinction, absorption, albedo, $\langle \cos(\theta) \rangle$, and $\langle \cos^2(\theta) \rangle$ have been calculated for wavelengths from 1 cm (30 GHz) to 1 Å (12.4 keV), for selected mixtures of carbonaceous grains and

⁶www.astro.princeton.edu/draine/dust/dustmix.html

amorphous silicate grains. These models cover three values of R_V , 3.1, 4.0, and 5.5.

The required input for both extinction models is A_V . In Section 2.3 we explain how the code estimates A_V in the line of sight of each star.

2.5 Observing condition

As explained earlier, MYOSOTIS provides a customized list of telescope filters. In addition to the filter transparency, MYOSOTIS needs to know the pixel-scale and the angular resolution of the observing instrument. If the telescope is ground-based (**Adaptiveoptics = ‘yes’**), then the user should also provide the atmospheric conditions, e.g. SR and the seeing values. If the ground-based telescope does not have any adaptive optics and its optimum resolution is poorer than seeing, user can simply choose an angular resolution equal to the seeing. The distance to the centre of mass of the object (e.g. star cluster) and the FOV should be also provided by the user. Note that all stars will not have the same distance from the observer as MYOSOTIS calculates the exact distance of each star, according to its 3D position. It is also possible to change the orientation of the object according to the observer’s line of sight. Our tool can apply the Doppler shift on the spectra of each star, according to its 3D velocity. Moreover, one can chose different values of signal-to-noise ratio (SNR) for the faintest star in the FOV. In this case MYOSOTIS will provide an extra FITS image with noise.

3 APPLICATIONS

To show some of the basic applications of MYOSOTIS, we simulated four star clusters using the publicly available code NBODY6 (Aarseth 1999). The initial conditions for these simulations are given in the following section. We generated synthetic observational data from these star clusters, using MYOSOTIS. Then we analyse these data step by step using standard photometric methods to:

- (1) extract stellar sources in each image
- (2) find common stars between the data sets in different wavelengths
- (3) fit isochrones to the CMD in order to estimate the age of the star cluster
- (4) estimate stellar masses in different filters in a given age
- (5) apply artificial stellar source recovery tests, to estimate the completeness as a function of stellar mass
- (6) plot mass functions and find the derived slope of the IMF in our synthetic images

For one of our simulations (Sim5), we embedded the stars within a cloud of SPH particles, to demonstrate the ability of MYOSOTIS to treat patchy extinction. Details of the cloud are given below in Section 3.2.

For one of our simulations (Sim1) we also show a small region from the centre of cluster, and compare the true positions of the stars with those derived from the photometry. In addition, we use this region to show how MYOSOTIS can be used to investigate blending in stellar spectra.

3.1 N-body simulations of star clusters

We use NBODY6 to simulate the dynamical and stellar evolution of four different clusters. The clusters are set up using MCLUSTER

Table 1. Initial conditions of the simulated clusters generated using MCLUSTER. Sim5 is the same as Sim1 except that in the generation and the analysis of the Sim5 synthetic images, the extinction due to a natal cloud is also taken into account.

ID	M_{tot} (M_{\odot})	R_h (pc)	Binary fraction (per cent)
Sim1	10^4	0.5	0
Sim2	10^4	0.5	50
Sim3	10^5	0.8	0
Sim4	10^5	0.8	30
Sim5 (Sim1 + gas)	10^4	0.5	0

(Kupper et al. 2011). Table 1 summarizes the initial conditions of the simulated clusters. As shown in the table, the simulated clusters differ in total initial mass (10^4 and $10^5 M_{\odot}$), half-mass radius (0.5 and 0.8 pc), and binary fraction (0, 30, and 50 per cent). We have used a Plummer model (Plummer 1911) for the initial mass density profile of these clusters. The IMF of stellar populations are taken from the distribution given by Kroupa (2001), with a mass range of 0.1–150 M_{\odot} .

The clusters are initially in virial equilibrium and there is no initial mass segregation.

For simulations with an initial binary population, the adopted algorithm (in MCLUSTER) for the pairing of primary and secondary components is as follows. The stars, with a Kroupa (2001) IMF, are split into two mass ranges by introducing a mass threshold of $5.0 M_{\odot}$. Stars whose mass is below or above this threshold are only paired randomly with stars which belong to the same mass range. This is in rough agreement with the findings of Kobulnicky & Fryer (2007). The period distribution of binaries for the low-mass population ($m < 5.0 M_{\odot}$) was obtained using the period distribution of Kroupa (1995), and for massive stars ($m > 5.0 M_{\odot}$) it is based on the distribution reported by Sana & Evans (2011). The semimajor axis distribution is obtained from the aforementioned period distributions. The eccentricity (e) for low-mass binaries is drawn from a thermal eccentricity distribution, i.e. $f(e) = 2e$ (e.g. Duquennoy & Mayor 1991; see also Kroupa 2008), whereas for the high-mass binaries it is from the Sana & Evans (2011) eccentricity distribution.

3.2 Generating synthetic images

For each simulated cluster we took one snapshot of the N -body simulations at the age of 2 Myr and created the synthetic observations using MYOSOTIS. The clusters are located at the distance of R136 in the large magellanic cloud (LMC, 50 kpc from Pietrzyński et al. 2013). Although R136 has a metallicity index of $[M/H] = -0.5$ as appropriate for LMC (Dufour 1984), we adopt a Solar metallicity for all simulated clusters, as the current version of MYOSOTIS is limited to only Solar metallicities at present.⁷ However, this will not affect our results since for the analysis of the photometric data we use the same metallicity that we use for the generation of the synthetic images. Thus, the general trend of our results (flattening of the observed MF; see Section 3.3) will not change as a function of metallicity.

The synthetic images have an FOV of $16 \text{ arcsec} \times 16 \text{ arcsec}$ which corresponds to $4 \text{ pc} \times 4 \text{ pc}$. All *HST*/WFPC2 images have a pixel scale of 50 mas and an angular resolution of 110 mas in

⁷Later versions will include the option to tailor metallicity values.

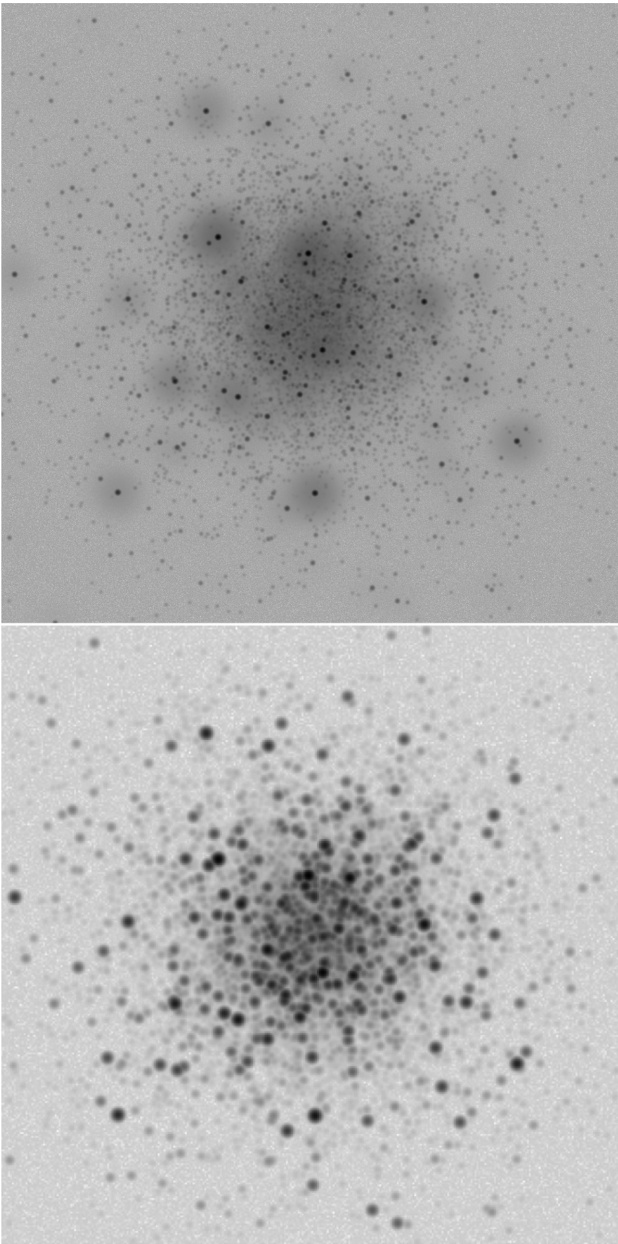


Figure 3. Synthetic images created from an N -body simulation (Sim1 in Table 1) at the age of 2 Myr. Top: VLT/SPHERE/IRDIS image in nearIR (K_s) with SR = 0.75 and seeing = 0.8 arcsec. Bottom: HST/WFPC2 in visible ($F555W$). The FOV of images is 16 arcsec \times 16 arcsec, covering 4 pc \times 4 pc.

the visible ($F555W$ filter). For VLT, we simulated SPHERE/IRDIS images in the nearIR (K_s) with a pixel sampling of 12.25 mas and an angular resolution of 64 mas. For the atmospheric models of O- and B-type stars in the FOV, we have chosen the OB treatment option (see Section 2) in MYOSOTIS. For VLT images, we considered the atmospheric condition, SR to be 0.75 and a seeing halo of 0.8 arcsec. In all the images we applied the shot noise of the sky such that the SNR is 2 for the faintest star in the FOV. Fig. 3 shows the simulated images of Sim1 in the nearIR, IRDIS/ K_s (top) and in the visible, WFPC2/ $F555W$ (bottom).

For simulations Sim1 to Sim4 we did not consider any extinction, meaning, that there is no gas nor dust in the line of sight connecting the observer to the stars. This enables us to examine the sole effect

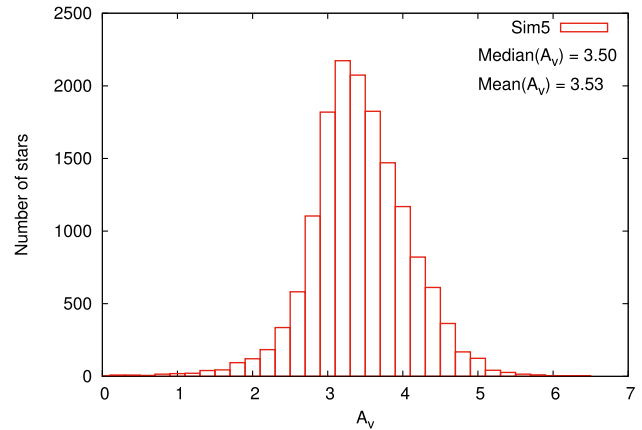


Figure 4. The histogram of extinction (A_V) in front of each stellar sources in Sim5 simulation. See Table 1 for the initial conditions of the simulations.

of angular resolution on the MF without being concerned about extinction. Sim5 cluster is embedded in its natal cloud which is homogeneous. The centre of the cloud is located in the centre of the cluster. We generated the cloud using the SPH code GANDALF (Hubber & Rosotti 2016; Hubber, Rosotti & Booth 2018). The cloud contains 10^5 SPH particles with smoothing lengths estimated by GANDALF. The total mass of the cloud is $4 \times 10^3 M_\odot$ which is ~ 40 per cent of the total mass of the star cluster. Fig. 4 shows the histogram of the extinction in front of each stellar source in Sim5. The average value of A_V is 3.5 but depending on the position of the stars in the cloud it varies between 0.2 and 5.8 mag. This value of A_V is small compare to the A_V of the Galactic YSCs. As an example, NGC 3603 has measured $A_V \sim 4.5$ (Khorrami et al. 2016) and Westerlund 1 has $A_V \sim 11.4$ (Damineli et al. 2016). See Sections 2.4 and 2.3 for more information on how MYOSOTIS estimates column density and extinction in front of each star, using the mass and smoothing length of cloud particles provided by GANDALF.

3.3 Photometric analysis and MF determination

We used STARFINDER (Diolaiti et al. 2000) to extract the stellar sources from the synthetic images. STARFINDER is a suitable code for the deep analysis of stellar fields, designed for AO images with high and low SR. The threshold for the photometry in our analysis was chosen to be 4σ above the sky noise. The minimum value of correlation between an acceptable stellar source and the input PSF was chosen to be 0.5 (see section 3.4 in Diolaiti et al. 2000 for more information). Table 2 shows the number of extracted sources and also the lowest mass estimated from the photometry ($m_{\text{low-obs}}$) on the synthetic images. Note that the noise of the sky has a different value in each synthetic image. As an example Sim1, Sim2 and Sim5 have same initial mass and the true number of stars in the image regions is about the same. However, a larger number of sources is extracted from Sim5 since its images have lower sky noise. Last column in Table 2 shows the SNR value for a $1 M_\odot$ star in each synthetic image. VLT/ K_s images have higher angular resolution and better pixel-sampling than HST/ V , and so more sources are detected in the VLT/ K_s images compare to the HST/ V images. The last two columns in Table 2 show the fraction of detected sources from the photometry versus both the real number of stars used to make the image (fourth column) and also the stars more massive than $m_{\text{low-obs}}$ (fifth column). In all cases, less than 47 per cent of stars above the photometric threshold could be

Table 2. The observed number of stars (N_{obs}) and the lowest mass observed ($m_{\text{low-obs}}$) in the photometric analysis. $\frac{N_{\text{obs}}}{N_{\text{total}}}$ shows the fraction of observed sources versus real number of stars used to create the synthetic image. $\frac{N_{\text{obs}}}{N_{(m>m_{\text{low-obs}})}}$ shows the fraction of observed sources versus the real number of stars more massive than $m_{\text{low-obs}}$. SNR is the signal to noise ratio of a $1 M_{\odot}$ star in the FOV of each image. For Sim5, the average value of extinction ($A_V = 3.53$) is considered in front of the $1 M_{\odot}$ star.

ID/telescope/filter	N_{obs}	$m_{\text{low-obs}}$ (M_{\odot})	$\frac{N_{\text{obs}}}{N_{\text{total}}}$	$\frac{N_{\text{obs}}}{N_{(m>m_{\text{low-obs}})}}$	SNR for $1 M_{\odot}$
Sim1/VLT/ K_s	3087	$0.33^{+0.20}_{-0.10}$	0.202	0.462	12.46
Sim1/HST/V	1322	$0.33^{+0.11}_{-0.10}$	0.086	0.198	74.47
Sim2/VLT/ K_s	3268	$0.33^{+0.20}_{-0.10}$	0.207	0.460	12.46
Sim2/HST/V	1433	$0.33^{+0.11}_{-0.09}$	0.091	0.202	74.47
Sim3/VLT/ K_s	9842	$0.68^{+0.15}_{-0.03}$	0.102	0.357	8.07
Sim3/HST/V	3558	$0.53^{+0.12}_{-0.00}$	0.037	0.093	26.18
Sim4/VLT/ K_s	10007	$0.68^{+0.15}_{-0.03}$	0.102	0.351	8.07
Sim4/HST/V	3586	$0.55^{+0.10}_{-0.02}$	0.037	0.095	26.18
Sim5/VLT/ K_s	3746	$0.16^{+0.55}_{-0.01}$	0.245	0.320	25.95
Sim5/HST/V	2119	$0.12^{+1.05}_{-0.01}$	0.138	0.150	905.48

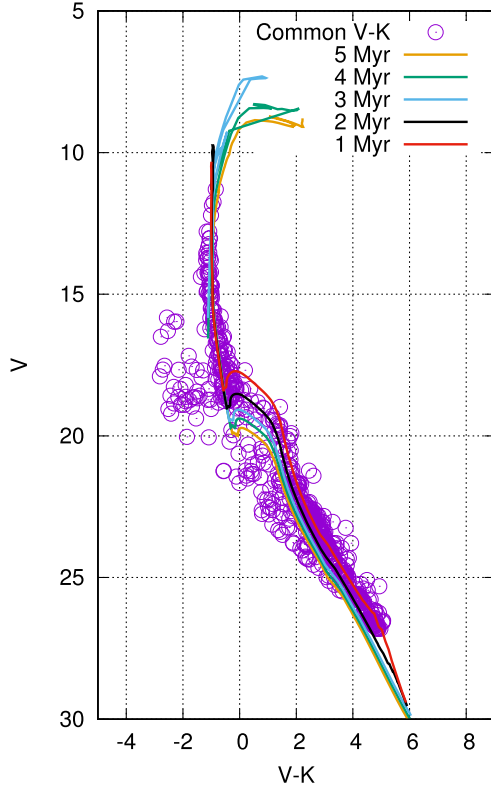


Figure 5. Colour magnitude diagram of Sim1 within *HST/F555W* and *IRDIS/ K_s* filters. Violet circles show the common sources (747) detected between two images. Solid lines are the PARSEC isochrones at different ages.

detected from the photometry. For one of the simulations (Sim1) we found the common sources between two sets of data in *HST/F555W* and *IRDIS/ K_s* filters. Fig. 5 shows the colour magnitude diagram (CMD) for these common sources. Among 3087 detected sources in K_s and 1322 in *F555W*, we could find 747 common sources. Solid lines in this figure are the PARSEC isochrones at 1, 2, 3, 4, and 5 Myr. The 2 Myr isochrone fits well with the CMD of the observed data. The conjunction of pre-main-sequence and main-sequence stars is

Table 3. MF slope (Γ) given in equation (4) for the simulated clusters. Γ_{real} : MF slopes derived directly from N -body simulations. Γ_{K_s} , Γ_V : MF slopes from the photometric analysis on the synthetic images of SPHERE/*IRDIS/ K_s* and *HST/WFPC2/F555W*, respectively. The low-mass limit for MF fitting is $2 M_{\odot}$ and C is the completeness value at this limit. The MF slopes are corrected for completeness and fitted with expected errors due to Poisson noise.

ID	Γ_{real}	Γ_{K_s}	C (per cent)	Γ_V	C (per cent)
Sim1	-1.29 ± 0.04	-1.13 ± 0.08	96	-0.95 ± 0.10	88
Sim2	-1.30 ± 0.05	-1.17 ± 0.05	95	-0.93 ± 0.08	94
Sim3	-1.29 ± 0.03	-0.98 ± 0.03	74	-0.82 ± 0.04	56
Sim4	-1.32 ± 0.02	-1.04 ± 0.04	75	-0.86 ± 0.04	63
Sim5	-1.29 ± 0.04	-1.09 ± 0.07	96	-0.59 ± 0.05	87

the best area to fit the isochrone, for YSCs which does not have horizontal branches (from evolved stars) at the upper part of the CMD.

We used PARSEC isochrone at 2 Myr to estimate the stellar masses. We considered a photometric error of $\sigma_{\text{mag}} = 0.2$ mag on the apparent magnitude of the detected sources. This corresponds to the average flux error of the extracted sources and provides us with an error on the stellar masses (σ_m). The uncertainty in the mass of each star was accounted for when constructing the MF. We estimated the slope of the MF (Γ) defined by equation (4),

$$\log_{10}(N) = \Gamma \log_{10}\left(\frac{m}{M_{\odot}}\right) + \text{constant}. \quad (4)$$

where m is the stellar mass and N is the number of stars. We used an implementation of the non-linear least-squares Marquardt–Levenberg algorithm to calculate the value of Γ for each cluster.

We performed incompleteness tests on each synthetic image by adding artificial stars with known magnitudes, one by one, to the synthetic images. These experiments were repeated 500 times for each flux value (magnitude). The completeness-corrected MF slopes are estimated for each simulation and the values are given in Table 3. The expected errors due to Poisson noise are considered in these fittings. The low-mass limit for fitting MF is $2.0 M_{\odot}$ and the completeness values for that mass are provided in Table 3. We fix the low-mass limit for all the synthetic images for the sake of the

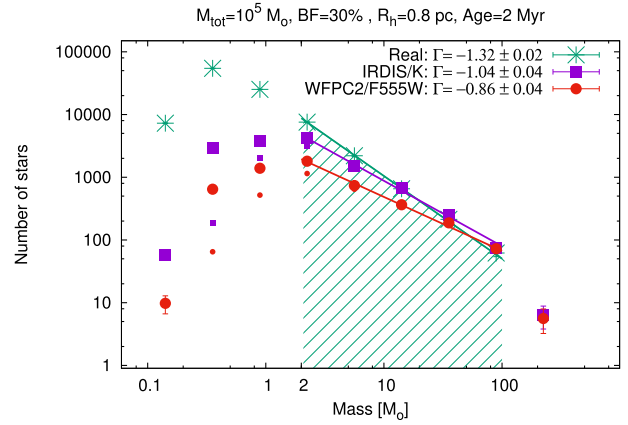
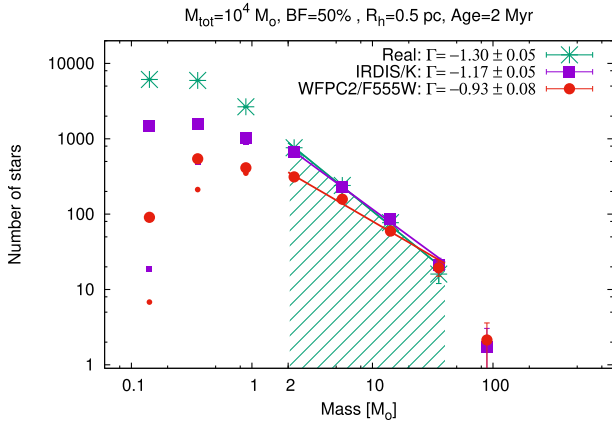
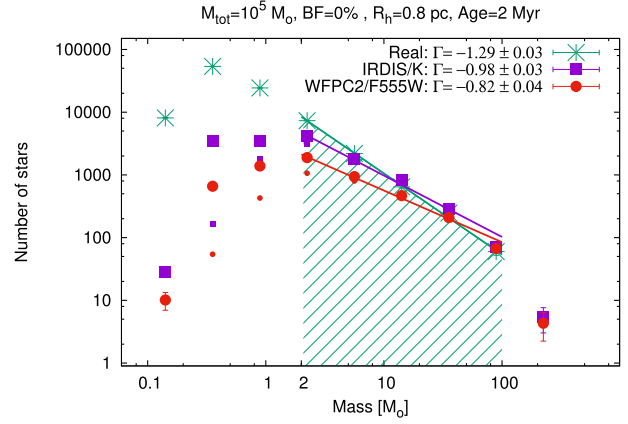
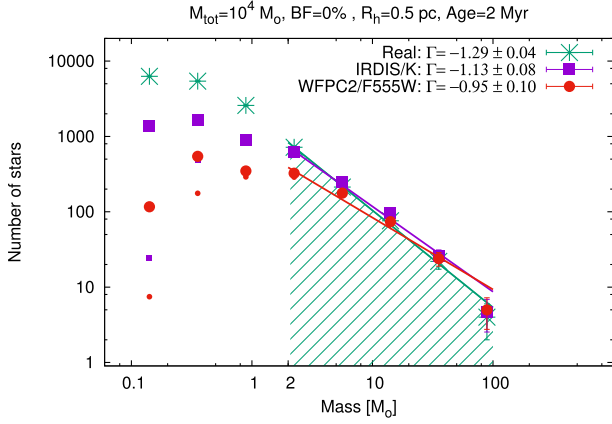


Figure 6. MF of Sim1 (top) and Sim2 (bottom) simulations, shown in Table 1 at the age of 2 Myr. Green is the MF derived directly from N -body simulations. Violet and red are the MF derived from the photometric analysis of the synthetic images created in SPHERE/IRDIS/ K_s filter and HST /WFPC2/F555W filter, respectively. Both clusters are non-segregated with initial total mass of $10^4 M_\odot$ and a half-mass radius of 0.5 pc. Top has no initial binaries and bottom has 50 per cent initial binaries. Small circles/squares are the number of detected sources and large circles/squares are their completeness-corrected values. Green filled area shows the mass range where MF is fitted.

Figure 7. Same as Fig. 6 but for Sim3 (top) and Sim4 (bottom). Both clusters are non-segregated with an initial total mass of $10^5 M_\odot$ and a half-mass radius of 0.8 pc. Top has no initial binaries and bottom has 30 per cent initial binaries.

MF slopes comparison. The completeness is above 50 per cent at this limit in all the images. The high-mass limit for the MF fitting is the last point where there is a star in the underlying MF. Figs 6–8 illustrate the MFs of all the simulated clusters. Small circles/squares are the observed number of stars and large circles/squares are their completeness-corrected values. Green filled area shows the mass range where MF is fitted. One can see that the measured MFs of the simulated clusters is lower (higher) than their underlying MFs at the low-mass (high-mass) end. This is due to the fact that, at low resolution the observed flux of some of the low-mass stars falls below the detection threshold, leading to an underestimation of low-mass stars. In addition, stars which are close to each other will be counted as one for a low resolution (crowding effect), leading to an overestimation of more massive objects.

Table 3 shows the MF slopes derived directly from N -body simulations (Γ_{real}) and also from the photometry of the synthetic images (Γ_{K_s} and Γ_V). The MF slopes of the clusters estimated from the synthetic images with low resolution (HST /F555W) are flatter than those with a higher resolution (SPHERE/IRDIS/ K_s) as well as the underlying MFs derived from the N -body simulations. As explained earlier, this is due to the fact that we underestimate

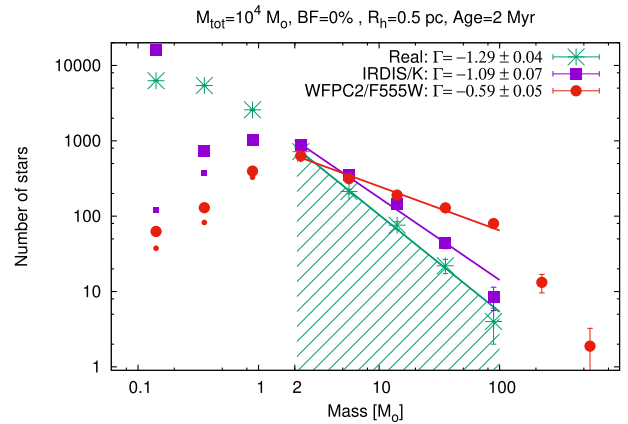


Figure 8. Same as Fig. 6 but for Sim5. The cluster is non-segregated with an initial total mass of $10^4 M_\odot$ and a half-mass radius of 0.5 pc and no initial binaries. This cluster contains gas with the average extinction of $A_V = 3.5$.

(overestimate) the number of low-mass (high-mass) stars as a result of low resolution. Therefore, as observational conditions become poorer, the observed MF becomes flatter, mimicking mass-segregation.

Sim5 is embedded in a homogeneous cloud and has a variable extinction (see Fig. 4) throughout the cloud as each star has a different distance from the observer. In the photometric analysis of the real observational data from star clusters, the extinction

is often considered to be a constant value which is applied to all detected sources in the FOV. If we consider a mean value of A_V (3.5 mag) for Sim5 in our photometric analysis, the stellar mass estimation would be affected significantly. As it can be seen from Table 3 and Fig. 8, among all the simulated clusters, Sim5 has the shallowest observed MF. In particular, Sim5 has an underlying MF slope of $\Gamma_{\text{real}} = -1.29 \pm 0.04$ and $\Gamma_V = -0.59 \pm 0.05$ from *HST*/WFPC2/*F555W* images. This is because we take the mean value of A_V for all the stars. As a result, some objects will have an overestimated (underestimated) A_V making them overluminous (underluminous) and thus more (less) massive, explaining the very different shape of the MF for sim5. Given the fact that Sim5 has the same observational conditions as Sim1 with the addition of extinction, and that the MF slope of Sim5 is ~ 0.4 dex shallower than that of Sim1 in the visible, indicates that extinction has a major effect on the measured MF slopes of YSCs.

According to Table 3, binaries do not affect the high-mass slope of the MF significantly. Note that the initial pairing of binary systems can affect the MF in addition to the observational biases.

3.4 Spectroscopy

Fig. 9 shows the synthetic spectroscopic data produced by MYOSOTIS from the centre of Sim1 cluster. MYOSOTIS created a cube of this region (FOV of $0.5 \text{ arcsec} \times 0.5 \text{ arcsec}$) so that the spectra along each pixel is available. The image has the angular resolution of *HST*/WFPC2 ($\sim 0.110 \text{ arcsec}$) in the *HST*/*F450W* filter and the spectroscopic resolution ($\lambda/\Delta\lambda$) of 700 covering wavelengths (3900–5100) Å. Creating the spectroscopic cube is computationally expensive so as an example we just created a small FOV with low spectral resolution data. The Doppler shift on the star's spectra from their velocity were not applied (although this is a feature in MYOSOTIS), so that we can demonstrate the effect of pure blending on the observational data.

In this small region there are 327 stars (green dots in Fig. 9). 25 stars have masses above $1 M_{\odot}$ (green stars in Fig. 9) and 5 of them are O- and B-type stars (green squares in Fig. 9) with $T_{\text{eff}} > 15000 \text{ K}$. The large blue circles in Fig. 9 shows the detected sources from the photometric analysis. Table 4 shows the magnitude and position (first and second columns) of B- and O-type stars in this FOV, compared to the magnitude and position derived from photometric analysis (third and fourth columns). One can see how poorly an observer can detect stellar sources. Among 327 stars just 4 of them are detected. None of the medium- and low-mass stars are detected in this region, and we have trouble detecting even the close-by massive stars.

We plotted an example of the spectra on the pixel highlighted with the black square. This is a pixel where the most massive star, in this FOV, is located (first star in Table 4). The comparison between low-resolution observed flux created by MYOSOTIS and the SED of the brightest star ($T_{\text{eff}} = 32500 \text{ K}$ and $\log g = 4.25$) from TLUSTY is shown in Fig. 9. This SED is chosen by MYOSOTIS according to the metallicity, mass and age of this star (see Section 2.1 on how MYOSOTIS chooses the proper SED for stars). The green line in Fig. 9 shows the SED of the brightest star observed at the distance of 50 kpc and multiplied by the chosen filter transparency.

The observed flux is higher than that of the brightest star's intrinsic flux, and the spectrum also has a different shape. This is because the observed flux is blended with the nearby detected sources, as well as an undetected early B-type star) and numerous undetected

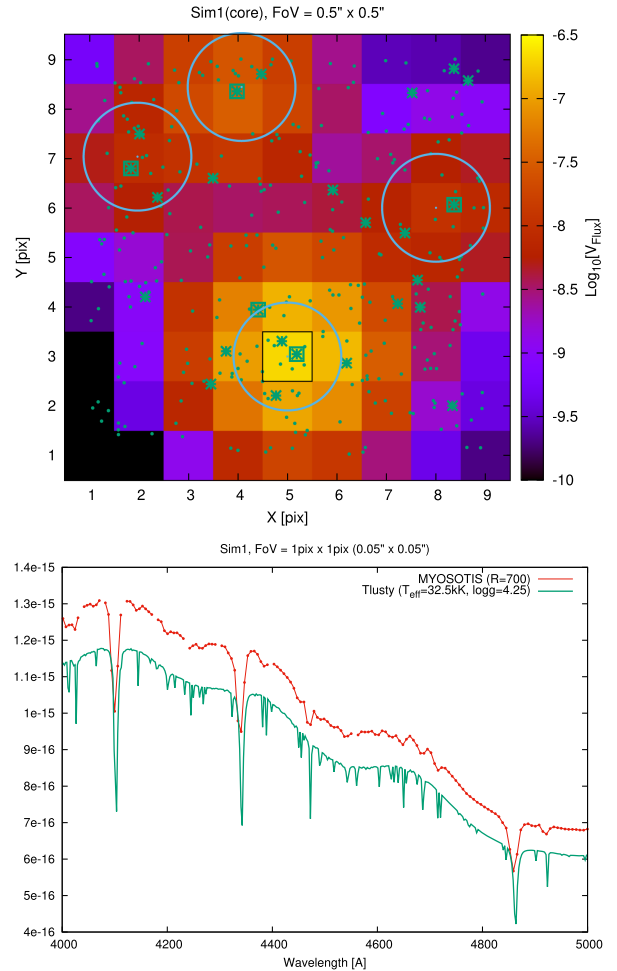


Figure 9. Top: Centre of Sim1 star cluster (FoV = $0.5 \text{ arcsec} \times 0.5 \text{ arcsec}$). MYOSOTIS created a cube of this region so that the spectra along each pixel is available. Stars with masses below $1 M_{\odot}$ are shown with a small dots. $1.0\text{--}3.5 M_{\odot}$ stars are shown with the star signs. The OB stars ($T_{\text{eff}} > 15 \text{ kK}$) are shown with the green squares. Large blue circles shows stars detected from the photometric analysis. Bottom: shows the example of spectra along the black pixel where the most massive star in the FoV is located. Red is a low-resolution spectra created by MYOSOTIS and Green is a TLUSTY SED for the represented star at the distance of 50 kpc in *HST*/*F450W* filter.

Table 4. Magnitude and position of B- and O-type stars in Fig. 9 are shown in the first and second columns. The photometric magnitude and positions (large blue circles in Fig. 9) are given in the third and fourth columns.

mag_{F555W}	$X \text{ (pix)}, Y \text{ (pix)}$	mag_{phot}	$X \text{ (pix)}, Y \text{ (pix)}$
14.8956	5.1893, 3.0490	14.894	5.000, 3.000
16.9248	3.9822, 8.3474	16.877	4.075, 8.436
18.3018	4.4093, 3.9458	—	—
18.3018	8.3662, 6.0624	18.561	8.000, 6.000
18.5249	1.8390, 6.7939	18.435	1.974, 7.032

medium- and low-mass stars. This demonstrates how MYOSOTIS can be used to examine the spectroscopic properties of stellar systems in clusters.

4 SUMMARY AND CONCLUSIONS

In this paper we introduced MYOSOTIS (Make Your Own Synthetic Observations), an IDL⁸ code written tool for simulating synthetic observation for space or ground-based telescopes which can synthesize both imaging and spectroscopic data. MYOSOTIS can generate the synthetic images from user input (given the position, age, and the mass of stars as well as the extinction values for the FOV) or from the output of N -body simulations (e.g. NBODY6) as well as SPH simulations (e.g. GANDALF). It uses the PARSEC evolutionary models and different atmosphere models to estimate the flux of stellar sources in different filters within a given FOV (see Section 2.1). The observing conditions, instrumental resolution and noise can be specified by the user (Section 2). MYOSOTIS is a highly customizable tool, with the user being able to define their own input models, such as filters, models for stellar evolution, stellar atmospheres, etc. The MYOSOTIS library of SEDs and evolutionary models can also be replaced easily to the updated models by the user. For example the high-resolution spectroscopic data from GAIA can be used as an input for different spectral type stars.

As an example of the application of MYOSOTIS in this paper, we created synthetic *HST*/WFPC2/*F555W* and *VLT*/SPHERE/*IRDIS/K_s* images of five YSCs at the age of 2 Myr with Solar metallicity, in the visible and nearIR. Each cluster had a different initial total mass, half-mass radius, binary fraction, and extinction. Photometry on each image was done using STARFINDER package. We used PARSEC evolutionary models for re-estimating cluster's age by isochrone fitting on the CMD. The stellar masses are re-estimated using 2 Myr PARSEC isochrone and the average value of the extinction in the FOV. The underlying MF and the observed MF of each cluster (subject to different observing conditions) was derived by considering the error on stellar masses. We also performed the artificial star test on each synthetic image to estimate the completeness-corrected MF slopes (Table 3). In all the cases, the slope of the MF (Γ) becomes flatter as the resolution decreases. All MF slopes of the *HST* synthetic images are flatter than those of SPHERE, which in turn are both flatter than the underlying MFs of YSCs obtained directly from N -body simulations. Standard completeness tests do not seem to help here. This is likely because they assume that stars are randomly positioned in the stellar field, while in clusters such as those we examine here, there is significant sub-clustering (even after 2 Myr of dynamical N -body evolution). This sub-clustering is not taken into account in the completeness tests, when randomly positioning the fake sources, and we so we tend to overestimate the completeness.

Moreover, according to our analysis, the difference between the measured MF of clusters with an initial binary population and those without binaries is ≤ 0.1 dex, i.e. the effect of binaries on the high-mass slope of the MF is marginal. This study suggests that the observed discrepancy in the reported values of the MF slopes of YSCs (such as R136 and NGC 3603) could primarily be due to how incompleteness is treated, rather than the unresolved binary population. However significantly more work needs to be done to see whether this is indeed the case. We aim to explore this in an upcoming paper.

Our analysis also confirms that extinction can have a major effect on the measured value of the MF slopes, especially at visible band wavelengths. In particular, we demonstrated that in the presence of

extinction the measured MF slope of a YSC in *HST*/WFPC2/*F555W* images is ~ 0.4 dex shallower compared to when there is no extinction (compare Sim5 with Sim1 in Table 3). The effect of resolution on both photometry and spectroscopy data can be seen in details in the example of spectroscopic-image cube from the centre of Sim1 (Fig. 9-top). Only 16 per cent (0.01 per cent) of stars with masses above $1 M_{\odot}$ ($0.1 M_{\odot}$) is detected by photometry. The spectra of a typical O-type star is blended with the nearby undetected sources (Fig. 9-bottom). This result suggests that the observed mass segregation reported for some YSCs (see MF slopes reported in Eisenhauer et al. 1998; Sung & Bessell 2004; Stolte et al. 2006; Harayama, Eisenhauer & Martins 2008; Pang et al. 2013; Khorrami et al. 2016 for NGC 3603 and Malumuth & Heap 1994; Brandl et al. 1996; Hunter et al. 1996; Massey & Hunter 1998; Selman et al. 1999; Sirianni et al. 2000; Andersen et al. 2009; Khorrami et al. 2017 for R136), could also be explained by observational confusion for the lack of angular resolution and unknown extinction values across the observed FOV. However more work would need to be done to support this conclusion.

In principle, the shape of MF for a given simulated cluster can be affected by binaries, multiple populations, patchy extinction, telescope limitations, and incompleteness estimates. MYOSOTIS can be used to investigate the effect of the above-mentioned parameters on the MF estimated from different observational instruments. It can also be used to explore the effects of age-determination. For example, a wrong estimation of the age of the star cluster, which can be caused by multiple stellar populations or extinction in very broad observing filters (e.g. *Gaia* g filter), will also have an effect on the derived MF. MYOSOTIS is also useful for projects such as studying multiple populations in star clusters, and their affect on observationally derived parameters. This could also be used to look at cluster merger events, where each cluster has different ages and/or metallicities. The physical properties of the binary (or multiple) systems measured from synthetic observations, can be compared with their original values from the simulations.

It should be stressed that for simulating clusters with extinction, MYOSOTIS is designed to look at the visible and near-infrared wavelengths where dust re-emission is not significant. When this approximation fails, one needs to resort to a more detailed radiative transfer approach (e.g. Koepferl, Robitaille & Dale 2017).

ACKNOWLEDGEMENTS

We would like to thank the reviewer for their constructive and insightful comments. The StarFormMapper project has received funding from the European Union's Horizon 2020 research and innovation programme under grant agreement no. 687528. This research has made use of the SVO Filter Profile Service (<http://svo2.cab.inta-csic.es/theory/fps/>) supported from the Spanish MINECO through grant AyA2014-55216. Paul C. Clark acknowledges support from the Science and Technology Facilities Council (under grant ST/N00706/1). Finally, we would also like to thank Lee G. Mundy for his suggestions which led to the improvement of this work.

REFERENCES

- Aarseth S. J., 1999, *PASP*, 111, 1333
 Allard F., Hauschildt P. H., Alexander D. R., Starrfield S., 1997, *ARA&A*, 35, 137
 Allison R. J., Goodwin S. P., Parker R. J., de Grijs R., Portegies Zwart S. F., Kouwenhoven M. B. N., 2009, *ApJ*, 700, L99

⁸The IDL version of the source code of MYOSOTIS is publicly accessible in <https://github.com/zkhorrami/MYOSOTIS>, and a PYTHON version is currently under development.

- Andersen M., Zinnecker H., Moneti A., McCaughrean M. J., Brandl B., Brandner W., Meylan G., Hunter D., 2009, *ApJ*, 707, 1347
- Bastian N., Covey K. R., Meyer M. R., 2010, *ARA&A*, 48, 339
- Baumgardt H., De Marchi G., Kroupa P., 2008, *ApJ*, 685, 247
- Brandl B. et al., 1996, *ApJ*, 466, 254
- Bressan A., Marigo P., Girardi L., Salasnich B., Dal Cero C., Rubele S., Nanni A., 2012, *MNRAS*, 427, 127
- Cai M. X., Kouwenhoven M. B. N., Portegies Zwart S. F., Spuzem R., 2017, *MNRAS*, 470, 4337
- Castelli F., Gratton R. G., Kurucz R. L., 1997, *A&A*, 318, 841
- Chatterjee S., Fregeau J. M., Rasio F. A., 2009, *BAAS*, 41, 331.02
- Chen Y., Bressan A., Girardi L., Marigo P., Kong X., Lanza A., 2015, *MNRAS*, 452, 1068
- Chen Y., Girardi L., Bressan A., Marigo P., Barbieri M., Kong X., 2014, *MNRAS*, 444, 2525
- Damineli A., Almeida L. A., Blum R. D., Damineli D. S. C., Navarete F., Rubinho M. S., Teodoro M., 2016, *MNRAS*, 463, 2653
- De Marchi G., Paresce F., Pulone L., 2007, *ApJ*, 656, L65
- Diolaiti E., Bendinelli O., Bonaccini D., Close L., Currie D., Parmeggiani G., 2000, *A&AS*, 147, 335
- Domínguez R., Fellhauer M., Blaña M., Farias J. P., Dabringhausen J., 2017, *MNRAS*, 472, 465
- Draine B. T., 2003a, *ARA&A*, 41, 241
- Draine B. T., 2003b, *ApJ*, 598, 1017
- Draine B. T., 2003c, *ApJ*, 598, 1026
- Dufour R. J., 1984, in Van den Bergh S., de Boer K. S. D., eds, *Proc. IAU Symp. 108, Structure and Evolution of the Magellanic Clouds*. Reidel, Dordrecht, p. 353
- Duquennoy A., Mayor M., 1991, *A&A*, 248, 485
- Eisenhauer F., Quirrenbach A., Zinnecker H., Genzel R., 1998, *ApJ*, 498, 278
- Espinoza P., Selman F. J., Melnick J., 2009, *A&A*, 501, 563
- Fitzpatrick E. L., 1999, *PASP*, 111, 63
- Giersz M., Heggie D. C., 2009, *MNRAS*, 395, 1173
- Girardi L., Bertelli G., Bressan A., Chiosi C., Groenewegen M. A. T., Marigo P., Salasnich B., Weiss A., 2002, *A&A*, 391, 195
- Güver T., Özel F., 2009, *MNRAS*, 400, 2050
- Harayama Y., Eisenhauer F., Martins F., 2008, *ApJ*, 675, 1319
- Hauschildt P. H., Allard F., Baron E., 1999, *ApJ*, 512, 377
- Heggie D. C., Giersz M., 2009, *MNRAS*, 397, L46
- Hubber D., Rosotti G., 2016, *Astrophysics Source Code Library*, record ascl:1602.015
- Hubber D. A., Rosotti G. P., Booth R. A., 2018, *MNRAS*, 473, 1603
- Hubeny I., Lanz T., 1995, *ApJ*, 439, 875
- Hunter D. A., O'Neil E. J., Jr, Lynds R., Shaya E. J., Groth E. J., Holtzman J. A., 1996, *ApJ*, 459, L27
- Hurley J. R., Shara M. M., 2012, *MNRAS*, 425, 2872
- Hurley J. R., Tout C. A., Pols O. R., 2002, *MNRAS*, 329, 897
- Kalirai J. S., Richer H. B., 2010, *Phil. Trans. R. Soc. A*, 368, 755
- Khalaj P., Baumgardt H., 2013, *MNRAS*, 434, 3236
- Khorrami Z. et al., 2016, *A&A*, 588, L7
- Khorrami Z. et al., 2017, *A&A*, 602, A56
- Kobulnicky H. A., Fryer C. L., 2007, *ApJ*, 670, 747
- Koepferl C. M., Robitaille T. P., Dale J. E., 2017, *ApJ*, 849, 1
- Kroupa P., 1995, *MNRAS*, 277, 1491
- Kroupa P., 2001, *MNRAS*, 322, 231
- Kroupa P., 2008, *LNP*, 760, 181
- Kupper A. H. W., Maschberger T., Baumgardt H., Kroupa P., 2011, *MNRAS*, 417, 2300
- Lada C. J., Lada E. A., 2003, *ARA&A*, 41, 57
- Lanz T., Hubeny I., 2003, *ApJS*, 147, 225
- Lanz T., Hubeny I., 2007, *ApJS*, 169, 83
- Li A., Draine B. T., 2001, *ApJ*, 554, 778
- Malkov O., Zinnecker H., 2001, *MNRAS*, 321, 149
- Malumuth E. M., Heap S. R., 1994, *AJ*, 107, 1054
- Massey P., Hunter D. A., 1998, *ApJ*, 493, 180
- Monaghan J. J., Lattanzio J. C., 1985, *A&A*, 149, 135
- Pang X., Grebel E. K., Allison R. J., Goodwin S. P., Altmann M., Harbeck D., Moffat A. F. J., Drissen L., 2013, *ApJ*, 764, 73
- Parker R. J., Goodwin S. P., Wright N. J., Meyer M. R., Quanz S. P., 2016, *MNRAS*, 459, L119
- Parker R. J., Reggiani M. M., 2013, *MNRAS*, 432, 2378
- Pietrzyński G. et al., 2013, *Nature*, 495, 76
- Plummer H. C., 1911, *MNRAS*, 71, 460
- Portegies Zwart S. F., McMillan S. L. W., Gieles M., 2010, *ARA&A*, 48, 431
- Priyatikanto R., Kouwenhoven M. B. N., Arifyanto M. I., Wulandari H. R. T., Siregar S., 2016, *MNRAS*, 457, 1339
- Rodrigo C., Solano E., 2013, *The Filter Profile Service Access Protocol*. Available at: <http://ivoa.net/documents/Notes/SVOFPS/index.html>
- Rodrigo C., Solano E., Bayo A., 2012, *The SVO Filter Profile Service*. Available at: <http://ivoa.net/documents/Notes/SVOFPS/index.html>
- Sana H., Evans C. J., 2011, in Neiner C., Wade G., Meynet G., Peters G., eds, *Proc. IAU Symp. 272, Active OB Stars: Structure, Evolution, Mass Loss, and Critical Limits*, p. 474
- Selman F., Melnick J., Bosch G., Terlevich R., 1999, *A&A*, 347, 532
- Sirianni M., Nota A., Leitherer C., De Marchi G., Clampin M., 2000, *ApJ*, 533, 203
- Stolte A., Brandner W., Brandl B., Zinnecker H., Grebel E. K., 2006, *AJ*, 132, 253
- Sung H., Bessell M. S., 2004, *AJ*, 127, 1014
- Tang J., Bressan A., Rosenfield P., Slemmer A., Marigo P., Girardi L., Bianchi L., 2014, *MNRAS*, 445, 4287
- van Albada T. S., 1968, *Bull. Astron. Inst. Netherlands*, 19, 479
- Weingartner J. C., Draine B. T., 2001, *ApJ*, 548, 296

This paper has been typeset from a $\text{\TeX}/\text{\LaTeX}$ file prepared by the author.